Exergetic analysis of the NASA Rotor 37 compressor test case

Ilyès Berhouni, Ilias Petropoulos, Didier Bailly

Exergetic Analysis of the NASA Rotor 37 Compressor Test Case

I. Berhouni - I. Petropoulos - D. Bailly

Department of Aerodynamics, Aeroelasticity, Acoustics, ONERA Meudon, France
ilyes.berhouni@onera.fr
ilias.petropoulos@onera.fr
didier.bailly@onera.fr

ABSTRACT

Classical performance investigations in turbomachinery flows rely on scalars computed with averaged total quantities at fixed stations, without a clear link between losses and their physical origins. Such links are clearer in exergy-based analyses, which provide decompositions between reversible/irreversible losses and between mechanical/thermal effects. An exergy balance adapted to rotating frames of reference was recently validated by ONERA on a propeller configuration with the in-house post-processing software FFX. This paper presents its application to the performance investigation of the NASA Rotor 37 compressor test case. Attention is given to the decomposition of irreversible losses due to shockwaves, viscous and thermal effects. The impact of considering an isothermal (rather than adiabatic) casing is then studied via its impact on the exergy balance components. Finally, a comparison is performed between the reference geometry and an in-house optimized variant, giving a clearer insight into the sources of performance improvement.

KEYWORDS

Compressor, Exergy balance, FFX, Design, Performance, Losses

NOMENCLATURE

$\dot{\mathcal{A}}'_{tot} = \dot{\mathcal{A}}'_{\phi} + \dot{\mathcal{A}}'_{\nabla T} + \dot{\mathcal{A}}'_{w}$ Rate of total anergy generation
$\dot{\mathcal{A}}'_{w} = T_\infty \int_{S_w} [\![\frac{1}{T}\mathbf{q}' + \rho\delta s(\mathbf{V}' - \mathbf{s_e}')]\!] \cdot \mathbf{n}' \, \mathrm{d}S$ Rate of anergy generation by shockwaves
$\dot{\mathcal{A}}'_{\nabla T} = -\int_{\mathcal{V}} \frac{T_\infty}{T^2}\mathbf{q}' \cdot (\nabla \mathbf{T})' \, \mathrm{d}\mathcal{V}$ Rate of anergy generation by thermal mixing
$\dot{\mathcal{A}}'_{\phi} = \int_{\mathcal{V}} \frac{T_\infty}{T}\phi' \, \mathrm{d}\mathcal{V}$ Rate of anergy generation by viscous dissipation
h Local channel height
H Channel height measured at the casing
M Mach number
$\dot{m}$ Mass flow rate
n Unit normal vector
p, ρ, T Static pressure, density and temperature
q Heat flux by conduction
r Position vector
S_b, S_o Body and non-solid surfaces limiting the control volume
$\mathbf{s_e} = \boldsymbol{\omega} \times \mathbf{r}$, Rotation velocity
e, s Mass-specific internal energy and entropy
$\mathbf{V}, \mathbf{V_r}$ Absolute and relative fluid velocity vector
$W\dot{\Gamma}' = \int_{S_o} (\rho u' V'_\infty \mathbf{V_r}' + \mathbf{V}'_\infty \cdot ((p - p_\infty)\overline{\overline{I}}' - \overline{\overline{\tau}}')) \cdot \mathbf{n}' \, \mathrm{d}S$ Rate of exergy that has to be provided/consumed so that the mechanical equilibrium in translation is respected

$\dot{\mathcal{X}}'_m = \int_{S_o} \left(\frac{1}{2}\rho(\mathbf{V}' - \mathbf{V}'_\infty)^2 \mathbf{V_r}' + (p - p_\infty)(\mathbf{V}' - \mathbf{V}'_\infty)\right) \cdot \mathbf{n}' \, \mathrm{d}S$ Rate of mechanical exergy outflow
$\dot{E}'_{qb} = -\int_{S_b} \mathbf{q}' \cdot \mathbf{n}' \, \mathrm{d}S$ Rate of thermal energy supplied by conduction through S_b
$\dot{\mathcal{A}}'_{qb} = -\int_{S_b} \frac{T_\infty}{T} \mathbf{q}' \cdot \mathbf{n}' \, \mathrm{d}S$ Rate of thermal anergy supplied by conduction through S_b
$\dot{\mathcal{X}}'_{qb} = -\int_{S_b} \left(1 - \frac{T_\infty}{T}\right) \mathbf{q}' \cdot \mathbf{n}' \, \mathrm{d}S$ Rate of thermal exergy supplied by conduction through S_b
$\dot{\mathcal{X}}'_{qo} = -\int_{S_o} \left(1 - \frac{T_\infty}{T}\right) \mathbf{q}' \cdot \mathbf{n}' \, \mathrm{d}S$ Rate of thermal exergy supplied by conduction through S_o
$\dot{\mathcal{X}}'_r = \int_{S_o} (\rho(\mathbf{V}' \cdot \mathbf{s_e}')\mathbf{V_r}' + \mathbf{s_e}' \cdot ((p - p_\infty)\overline{\overline{I}}' - \overline{\overline{\tau}}')) \cdot \mathbf{n}' \, \mathrm{d}S$ Power transferred from the solid body to the flow through torque
$\dot{\mathcal{X}}'_{th} = \int_{S_o} \rho \left(\delta e + p_\infty \delta \left(\frac{1}{\rho}\right) - T_\infty \delta s\right) \mathbf{V_r}' \cdot \mathbf{n}' \, \mathrm{d}S$ Rate of thermocompressible exergy outflow
$\delta(\,)$ Perturbation of a quantity relative to the reference state, = $(\,) - (\,)_\infty$
ϕ Dissipation rate per unit volume
$\tau'_{br} = \int_{S_b} (\overline{\overline{\tau}}' \cdot \mathbf{V_r}') \cdot \mathbf{n}' \, \mathrm{d}S$ Viscous rate of work in the relative reference frame on S_b
$\tau'_o = \int_{S_o} (\overline{\overline{\tau}}' \cdot (\mathbf{V}' - \mathbf{V}'_\infty)) \cdot \mathbf{n}' \, \mathrm{d}S$ Viscous rate of work associated to velocity perturbations on S_o
$(\,)_\infty$ Quantity $(\,)$ at freestream conditions
$(\,)'$ Quantity $(\,)$ projected in the relative frame

Introduction

Classical methodologies for performance evaluation in turbomachinery rely on scalars computed using an average of stagnation quantities over the plane of analysis. Alongside flow visualisations, these are the most common tools integrated in numerical design processes aiming at improving the global efficiency of the system investigated. However, such approaches do not provide a clear phenomenological link between performance degradations and physical phenomena occurring in the flow field, as the use of averaged quantities cannot be completely representative of the flow physics (Burdett and Povey, 2022). They are also incomplete, as the ideal case against which the efficiency is measured is usually considered to be isentropic or reversible. Thus, traditional figures of merit tend to miss a potential for mechanical work extraction linked to irreversibilities present in the flow, such as the frictional reheat effect (Kotas, 1985).

To better analyse the sources of loss in internal flows, Miller proposed an approach based on the mechanical work potential (Miller, 2013). It allows to estimate the mechanical work that could be recovered through an isentropic process in which the system stagnation pressure evolves towards its thermodynamic dead state stagnation pressure. However, it voluntarily omits the potential of mechanical work recovery through thermal transfers bringing back the system to its dead state temperature (referred to as thermal work potential by Miller). It is argued that, considering current turbine technology, this part is not of interest for the designer.

Another approach relies on the concept of exergy (Çengel and Boles, 2015) which allows to consider both mechanical and thermal effects in the flow. A first exergy-based method used to analyse external flow configurations was proposed by Arntz et al. and successfully used to evaluate the performance of classic or disruptive aircraft configurations (Arntz, 2014). This method is not however adapted to internal flows in a rotating frame of reference. This is an important limitation for the investigation of turbomachinery flows, as rotor configurations are often studied in a rotating frame of reference with a steady-state flow hypothesis. Fiore proposed an extension of the exergy balance to rotating reference frames, and applied it to turbomachine cases such as a two-stage rotating turbine configuration (Fiore, 2019). On the one hand however, the derived formulation relies on the flow exergy definition instead of the exergy definition (Çengel and Boles, 2015; Kotas, 1985; Berhouni et al., 2023a) which should be adopted when consid-

ering unsteady flow analyses. On the other hand, the derived equations were not expressed in their Arbitrary Lagrangian-Eulerian (ALE) form, and did not let the inertial terms appear as the momentum conservation equation did not intervene.

Recently, a new derivation of an exergy balance adapted to rotating reference frames was investigated and applied to the performance evaluation of a propeller configuration (Berhouni et al., 2023b). The present paper aims at presenting the application of this exergy balance to the numerical study of the performance of a compressor rotor with the post-processing code *FFX* (Far-Field eXergy) developed at ONERA. The theoretical balance is detailed in a first section, and then applied to the NASA Rotor 37 test case. The exergy-based performance analysis is presented in a second section, in which the reference case is studied with both an adiabatic and an isothermal casing. The adiabatic results are then compared with those obtained for an optimized geometry. A conclusion on the results obtained and the perspectives for future work are presented in the last section.

Exergy balance adapted to rotating frames of reference

The fluid flow analysis is carried out in a continuous volume $\mathcal{V}$ representative of a turbomachine rotor stage. The volume is limited by a non-permeable solid body surface S_b (composed of a rotor and a fixed casing) and an outer boundary S_o, as illustrated in Fig. 1. The control volume follows the movement of the rotor, which is in rotation at a velocity $\mathbf{s_e}$ with respect to the inertial fixed frame R_f, and a non-inertial relative frame R_r is attached to it. The rotating velocity is expressed as $\mathbf{s_e} = \boldsymbol{\omega} \times \mathbf{r}$, where $\boldsymbol{\omega}$ is the angular velocity. A vector pointing outwards of the volume and locally normal to its exterior surface is noted $\mathbf{n}$. The presence of a steady shockwave attached to the body is also considered through a surface of discontinuity S_w.

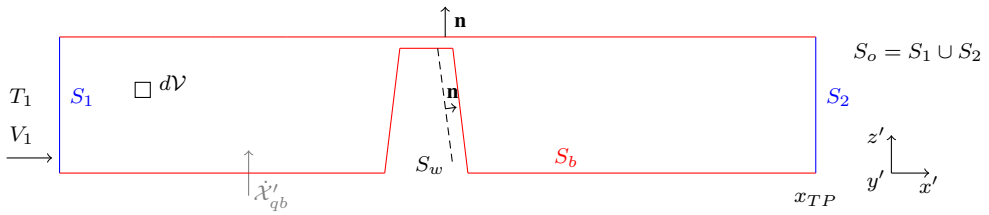

Figure 1: 2D cross section of a 3D control volume surrounding a turbomachine rotor

The system is thermodynamically open as it exchanges mass, work and heat with its surroundings across its boundaries. The analysis is carried out in R_r, where the control volume is fixed with the fluid flowing in and out of it. The no-slip boundary condition on the rotor surface is expressed as $(\mathbf{V}' - \mathbf{s_e}') = \mathbf{0}$, where the superscript $'$ indicates that the quantities are projected in R_r. The control volume extends up to a transverse plane placed at a fixed coordinate x_{TP}. In the rest of this paper, the fluid is considered a perfect gas and the flow investigated is steady in the rotating reference frame R_r. Additionally, the angular velocity is considered constant and oriented along the $\mathbf{x}$ axis (i.e. $\boldsymbol{\omega} = (\omega, 0, 0)^T$). Finally, the reference state velocity is defined along the rotation axis and the velocity perturbations in R_r are noted u',v' and w' (i.e. $\mathbf{V}' = (V'_\infty + u', v', w')^T$).

An exergy balance adapted to rotating frames of reference was recently developed and validated on a propeller configuration (Berhouni et al., 2023b), which takes the form:

$$\dot{\mathcal{X}}'_{qb} + \dot{\mathcal{X}}'_r + \tau'_{br} = W\dot{\Gamma}' + \dot{\mathcal{X}}'_m + \dot{\mathcal{X}}'_{th} + \dot{\mathcal{A}}'_\phi + \dot{\mathcal{A}}'_{\nabla T} + \dot{\mathcal{A}}'_w + \tau'_o - \dot{\mathcal{X}}'_{qo} \tag{1}$$

The Left-Hand-Side (LHS) terms of this balance represent the exergy transferred from the rotor to the fluid due to thermal conduction ($\dot{\mathcal{X}}'_{qb}$) and torque ($\dot{\mathcal{X}}'_r + \tau'_{br}$) on S_b. In the Right-Hand-

Side (RHS), the outflows of mechanical ($\dot{\mathcal{X}}'_m$) and thermocompressible ($\dot{\mathcal{X}}'_{th}$) exergy appear. They either represent a waste of exergy in the case where there is no device to convert it into mechanical work downstream (e.g. a turbine exhausting into the atmosphere) or a potential for mechanical work recovery if such a device is present (e.g. a compressor upstream of a turbine). Part of the exergy provided is dissipated by irreversible effects linked to anergy generation, such as viscous effects ($\dot{\mathcal{A}}'_\phi$), thermal mixing ($\dot{\mathcal{A}}'_{\nabla T}$) and shockwaves ($\dot{\mathcal{A}}'_w$). The two terms τ'_o and $\dot{\mathcal{X}}'_{qo}$ are respectively representative of variations in exergy outflow due to the viscous force rate of work and to thermal transfers by conduction on S_o.

A last term $W\dot{\Gamma}'$ appears in the RHS, which represents an exergy difference linked to the choice of a reference state velocity (i.e. the choice of M_∞) (Berhouni et al., 2023a). By selecting a value for the freestream velocity, a hypothesis is made that the configuration under study does not translate for an analysis done in a reference frame moving at the opposite of the corresponding freestream velocity V'_∞. $W\dot{\Gamma}'$ is the exergy that has to be provided/consumed so that the mechanical equilibrium in translation is respected.

Numerical application: NASA Rotor 37

Test case presentation

The NASA Rotor 37 geometry and a view of the surface mesh considered in this study are shown in Fig. 2. The case is a 36-blade isolated transonic axial compressor rotor, designed at NASA for experimental investigations (Reid and Moore, 1978; Moore and Reid, 1980; Suder, 1996) as an inlet stage for an eight-stage core compressor with a 20:1 pressure ratio. The data provided were used to validate turbomachinery-oriented CFD codes and numerical methods (Denton, 1997; Hah, 2009). In this study, a multiblock structured mesh composed of around 1.3 million points with 24 cell layers in the tip clearance area is used for the numerical computations. The blade surface mesh is composed of 77 points in the spanwise direction, and each radial section of the blade is discretized with 233 points in the chordwise direction. The y+ value over the blade is in the order of 0.8 for the high-flow operating regime corresponding to $\dot{m} \approx 0.98\dot{m}_{choke}$.

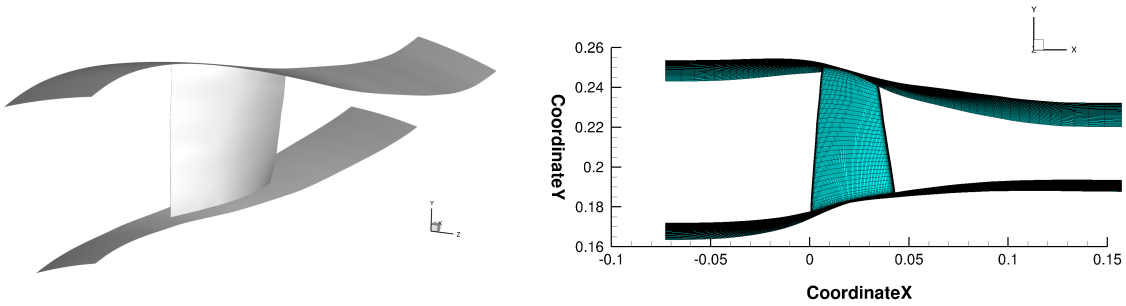

Figure 2: NASA Rotor 37 geometry (left) and side view of the surface mesh (right).

The numerical computations were carried out with the ONERA-SAFRAN CFD solver elsA (Cambier et al., 2013) on a 10-degree azimuthal section with periodic boundary conditions and a no-slip boundary condition applied at all solid boundaries. The ALE steady Reynolds-Averaged Navier-Stokes (RANS) in their relative velocity, relative frame formulation and supplemented by the one-equation Spalart-Allmaras turbulence model are solved in the numerical simulations. The angular velocity is fixed to its nominal value $\omega = 1780$ rad.s^{-1}. The compressor choke mass flow rate was estimated at $\dot{m}_{choke} = 20.82$kg.s^{-1} through an iterative process. The dead state used in the definition of exergy is chosen as the external freestream flow state. In particular, ρ_∞ = 1.225 kg.m^{-3} and T_∞ = 288.15K were chosen as the sea-level standard atmosphere con-

ditions consistently with the Rotor 37 test case, whereas M_∞ = 0.5 was chosen arbitrarily (this choice is further discussed in the following section). Choosing the external freestream flow state is physically consistent since the dead state is defined as the state in which the system is thermodynamically inert, but other options could have been selected such as choosing the reference state as the inlet flow thermodynamic state. This other option would however generally lead to additional issues for the exergy-based performance analysis. The most straightforward issue could appear in a case with multiple inlets, where an arbitrary choice would have to be made regarding which inflow to consider as the reference state. Another issue would arise when comparing the results to other turbomachine stages, as two different reference states corresponding to each configuration's inflow would be used and thus the exergy-based performance investigations could not be compared (or combined) easily. Choosing the reference state as the external aerodynamic state is thus deemed more consistent, as it can be considered constant between different engine elements. The computational domain extends in the x-direction from $x_{min} = -0.0728$m to $x_{max} = 0.15698$m, with the blade root situated approximately between $x = 0$m and $x = 0.045$m. The results obtained were then post-processed with the FFX exergy analysis software developed at ONERA (Berhouni et al., 2023b). This is coupled with the ONERA Cassiopée set of python modules for the pre- and post-processing of CFD computations (Benoit et al., 2015).

In this paper, the reference NASA Rotor 37 exergetic performance is also compared to results obtained for an ONERA in-house optimized geometry. The optimization was done using the elsA adjoint solver (Peter et al., 2015) with the linearized Spalart-Allmaras turbulence model. The descent method algorithm selected is the method of feasible directions from the DOT optimiser library (Vanderplaats), with gradients estimated by the adjoint method. The isentropic efficiency (chosen as the objective function) was then maximized with the pressure ratio constrained to remain above 2.0 for the high-flow operating regime (corresponding to $\dot{m} \approx 0.98\dot{m}_{choke}$). A second constraint was applied to an operating regime near choke ($\dot{m} \approx 0.9997\dot{m}_{choke}$), which imposed $\dot{m}$ to remain within 0.01 kg.s^{-1} of its reference value (i.e. 0.05% of $\dot{m}_{choke}$). Additionally, the evolution of the static pressure distribution at the outlet section was constrained for the two aforementioned operating regimes. The optimization led to a gain of performance by modifying the blade skeleton camber-line angle along the channel height with other structural design parameters remaining unchanged. Fig. 3 illustrates the parametrization of the blade for the optimization, as well as the camber-line angle modifications performed for three different channel height sections. The performance gain achieved with this optimization is investigated in details with the exergy balance in a further section.

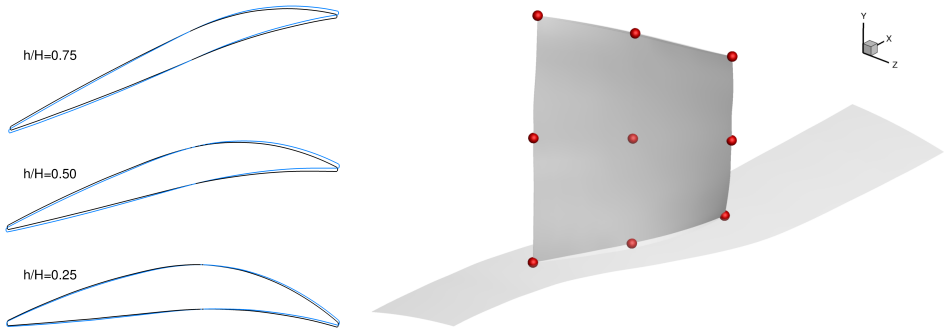

Figure 3: Blade profile modifications at different channel heights (left, geometry not to scale) and Akima spline control points of the blade for the optimization (right). The reference and optimized geometries are respectively colored in black and blue.

Preliminary considerations

No significant heat exchanges are considered through S_o, and as their negligible values are numerically confirmed, τ'_o, τ'_{br} and $\dot{\mathcal{X}}'_{qo}$ are neglected for this study. Eq. (1) is simplified to:

$$\dot{\mathcal{X}}'_{qb} + \dot{\mathcal{X}}'_r = \underbrace{W\dot{\Gamma}' + \dot{\mathcal{X}}'_m}_{\dot{\mathcal{X}}'_{m,tot}} + \dot{\mathcal{X}}'_{th} + \dot{\mathcal{A}}'_\phi + \dot{\mathcal{A}}'_{\nabla T} + \dot{\mathcal{A}}'_w \tag{2}$$

where $\dot{\mathcal{X}}'_{m,tot}$ is the total mechanical exergy outflow (equivalent to $\dot{\mathcal{X}}'_m$ when $\mathbf{V}'_\infty = \mathbf{0}$). As the performance is evaluated at different downstream transverse planes, the rate of exergy that has to be consumed for the axial mechanical equilibrium to be respected evolves (i.e. $W\dot{\Gamma}'$ varies), and so does the mechanical exergy outflow. Indeed, if less exergy has to be consumed to achieve the axial mechanical equilibrium, it means that more exergy is available downstream. This implies that a transfer between $W\dot{\Gamma}'$ and $\dot{\mathcal{X}}'_m$ must occur: in the case where $W\dot{\Gamma}'$ decreases when the transverse plane is located further downstream, $\dot{\mathcal{X}}'_m$ correspondingly increases. This transfer is however non-unique (a transfer also occurs between $\dot{\mathcal{X}}'_m$ and $\dot{\mathcal{X}}'_{th}$, e.g. due to a decrease of the flow section) and is strongly dependent on the reference velocity chosen (as is $W\dot{\Gamma}'$). Part of the exergy is also lost in the process due to irreversible losses in the flow, linked to anergy generation. Due to the above reasons, the introduction of $\dot{\mathcal{X}}'_{m,tot}$ is useful as its variations do not depend on the value chosen for $\mathbf{V}'_\infty$, but are only linked to transfers with $\dot{\mathcal{X}}'_{th}$ and to irreversible losses. In other words, the choice of $\mathbf{V}'_\infty$ only influences the repartition of $\dot{\mathcal{X}}'_{m,tot}$ between $\dot{\mathcal{X}}'_m$ and $W\dot{\Gamma}'$ as the mechanical exergy outflow can be rewritten as $\dot{\mathcal{X}}'_m = \dot{\mathcal{X}}'_{m,tot} - W\dot{\Gamma}'$. The decomposition between $W\dot{\Gamma}'$ and $\dot{\mathcal{X}}'_m$ is performed in the following for the sake of illustrating the evolution of these components, but it should be noted that it only fully makes sense when $\mathbf{V}'_\infty$ (i.e. the translation velocity of the body) is known (Berhouni et al., 2023a). In the following sections, the values of the exergy balance components are normalized in the form of non-dimensional coefficients as $C_{\dot{\mathcal{X}}'} = \frac{\dot{\mathcal{X}}'}{0.5\rho_\infty S_{ref} V'^3_\infty}$, and their non-dimensional values are given in power counts (pc, 10^{-4}).

Several exergy-based figures of merit can be defined to quantify the compressor efficiency:

$$\psi_p = \frac{W\dot{\Gamma}'}{\dot{\mathcal{X}}'_r + \dot{\mathcal{X}}'_{qb}} \qquad \psi_c = \frac{\dot{\mathcal{X}}'_m + \dot{\mathcal{X}}'_{th}}{\dot{\mathcal{X}}'_r + \dot{\mathcal{X}}'_{qb}} \qquad \psi_{cr} = \frac{W\dot{\Gamma}' + \dot{\mathcal{X}}'_m + \dot{\mathcal{X}}'_{th}}{\dot{\mathcal{X}}'_r + \dot{\mathcal{X}}'_{qb}} \tag{3}$$

where ψ_p, ψ_c and ψ_{cr} are respectively referred to as the propulsive, compression and reversible compression efficiency. ψ_p represents the part of the exergy provided by the compressor to the fluid that is consumed to maintain the current axial mechanical equilibrium. In other words, it expresses the part of the exergy provided that is converted to effective thrust. ψ_c is the exergy provided that is recovered at the exit of the turbomachine stage, which for a compressor is considered an exergy gain convertible into mechanical work in downstream stages of the engine (i.e. the turbine). These two figures of merit are highly dependent on the reference velocity chosen for the computation of the exergy balance. Indeed, the faster the moving speed of the configuration, the higher the exergy consumed to maintain the axial mechanical equilibrium (i.e. the higher ψ_p). This would correspond to less exergy available at the stage exit (i.e. a lower value of ψ_c). ψ_{cr} is then introduced, as it represents the efficiency that would be obtained if all the kinetic energy were to be convertible into mechanical work (case of a turbomachine tested at rest for example). This term is not dependent on the reference velocity chosen in the exergy definition, and represents the maximum value that can be attained by the compression

efficiency. In particular, if $\mathbf{V}'_\infty = \mathbf{0}$ (case of a ground test), $\psi_c = \psi_{cr}$ and $\psi_p = 0$.

In this paper, ψ_{cr} will be compared to the isentropic efficiency, computed as $\eta_{is} = \frac{\left(\frac{P_{i2}}{P_{i1}}\right)^{\frac{\gamma-1}{\gamma}} - 1}{\frac{T_{i2}}{T_{i1}} - 1}$. Such a comparison was investigated by (Kotas, 1985) and showed that the difference between exergy-based and isentropic efficiencies is due to effects linked to irreversibilities, such as friction reheat or thermal recool. Additionally, discrepancies can appear due to different sources of inaccuracy between ψ_{cr} (impacted by numerical flow field inaccuracies, e.g. numerical dissipation) and η_{is} (impacted also by the average performed for the total pressure P_i and temperature T_i). In this paper, the P_i and T_i values used to compute η_{is} are respectively energy-averaged and mass-averaged at the stations of interest, similarly to the NASA experiment (Suder, 1996). Contrary to the experimental strategy in which averaging was performed at 18 positions along the channel height, total quantity averages are computed over the complete station in the present study. This difference is expected to lead to overall lower η_{is} values compared to the experimental data, which underestimated losses in the annulus boundary layers (Denton, 1997).

Numerical results

High-flow condition ($\dot{m} \approx 0.98\dot{m}_{choke}$) with adiabatic walls

In this section, the exergy-based performance of the Rotor 37 is analysed for a high-flow condition, with the walls considered adiabatic (i.e. $\dot{\mathcal{X}}'_{qb} = 0$). The exergy balance is computed for a series of downstream limits of the control volume with the x-coordinate for each plane noted x_{TP}, which varies between -0.06m and 0.15m with a step of 0.01m. Two additional stations are added at $x = -0.0419m$ and $x = 0.1067m$, which correspond to the planes used for the aerodynamic analysis in the Rotor 37 experiments (Suder, 1996). The results obtained for the exergy balance components and the associated figures of merit are then plotted in Fig. 4.

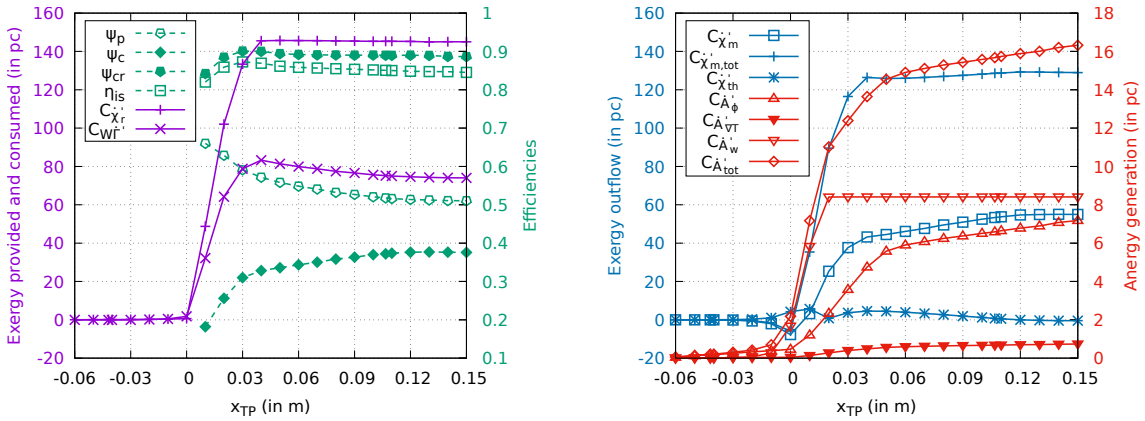

Figure 4: Evolution of the exergy balance components at $\dot{m} \approx 0.98\dot{m}_{choke}$.

The left graph shows that $C_{\dot{\mathcal{X}}'_r}$ and $C_{W\dot{\Gamma}'}$ are both very close to zero up to $x_{TP} = 0.0m$, since the contributions upstream of the blade are not significant for these terms. Moving the transverse plane further downstream leads to an increase of $C_{\dot{\mathcal{X}}'_r}$, until its maximum value of roughly 146 pc is obtained at the end of the inter-blade channel. Small variations of this quantity (below 1 pc) are then observed further downstream due to the motor and resisting torques linked respectively to the hub and the casing. Similarly, $C_{W\dot{\Gamma}'}$ reaches its maximum value of roughly 83 pc at the end of the inter-blade channel, the positive value obtained indicating that an excess of exergy has to be consumed for the configuration to maintain the mechanical equilibrium in translation

along x'. It then decreases when x_{TP} increases, in the same way as the streamwise resulting force due to a rearward component coming from the additional wall surface contained in the control volume. Part of this evolution comes from a transfer between $C_{W\dot{\Gamma}'}$ and $C_{\dot{\mathcal{X}}'_m}$, as a lower value of $C_{W\dot{\Gamma}'}$ corresponds to a higher value of exergy available to be converted into useful work (i.e. higher values of $C_{\dot{\mathcal{X}}'_m}$). The increase of mechanical exergy outflow is however not equal to the decrease of $W\dot{\Gamma}'$ due to transfers with $C_{\dot{\mathcal{X}}'_{th}}$ and additional irreversible dissipation is included in the control volume as the latter is extended downstream. Consequently to the evolution of $W\dot{\Gamma}'$ and $\dot{\mathcal{X}}'_r$, ψ_p decreases when x_{TP} increases. The compression efficiency on the other hand increases significantly in the inter-blade channel, and keeps increasing less steeply further downstream. This evolution highlights that a non-negligible amount of exergy is theoretically recoverable downstream of the compressor for this reference state. These two figures of merit are strongly impacted by the reference velocity chosen. The faster the configuration is assumed to translate, the lower are the values of the compression efficiency and the higher are those of the propulsive efficiency. The reversible compression efficiency gives an indication of the maximal compression efficiency that can be attained by the compressor, as it corresponds to the case of a compressor tested at rest (i.e. $V'_\infty = 0$). ψ_{cr} reaches its maximum value of 90% for $x_{TP} = 0.04$m, and then decreases as the transverse plane is moved downstream due to anergy generation in the flow field. The isentropic efficiency is also plotted on the left graph in Fig. 4 for comparison with ψ_{cr}. A similar trend between η_{is} and ψ_{cr} is obtained, with lower values for the isentropic efficiency which are due to the friction reheat effect and to different calculation methods for ψ_{cr} and η_{is} (the first is based on an exergy balance whereas the second on averages of total quantities).

The exergy outflow and anergy generated are then plotted on the right graph in Fig. 4. This shows that large variations for terms linked to mechanical effects occur when the transverse plane reaches the inter-blade channel. This is because the fluid is accelerated by the passage section reduction and rotated by the rotor, with several complex physical phenomena taking place (e.g. shockwaves, flow separation and tip leakage vortices). Overall, a significant increase of $C_{\dot{\mathcal{X}}'_m}$ is observed inside the inter-blade channel. Further downstream, $\dot{\mathcal{X}}'_m$ keeps increasing slowly, the major part of this increase being due to transfers with $C_{W\dot{\Gamma}'}$. This last observation is confirmed by the evolution of $C_{\dot{\mathcal{X}}'_{m,tot}}$ downstream of the blade (which is only due to transfers with $C_{\dot{\mathcal{X}}'_{th}}$ and anergy generation), which successively decreases and increases with lower variations than $C_{\dot{\mathcal{X}}'_m}$. Correspondingly, the thermocompressible exergy ouflow increases downstream of the blade before decreasing as the transverse plane is moved further downstream (due to the flow acceleration linked to the passage section reduction). A sudden drop of $\dot{\mathcal{X}}'_{th}$ is observed at $x_{TP} = 0.02m$, which is mostly due to a strong passage shock in the inter-blade channel. Consistently with these observations, the losses linked to irreversible effects in the flow increase as the transverse plane is moved downstream. A shock system is observed, consisting of a bow shock and a passage shockwave (with the bow shock waves propagating upstream of the blade) and complemented by a shock with a complex structure in the tip clearance area. Fig. 4 shows that the corresponding wave anergy increases to very low levels before the inter-blade channel is reached, meaning that losses due to the bow shock waves upstream are not significant. In the inter-blade channel, $C_{\dot{\mathcal{A}}'_w}$ increases significantly up to its maximum value of 8.41 pc for $x_{TP} = 0.02m$. This shows that for this position of the transverse plane, the complete shock system is included in the control volume, and so are the associated irreversible losses. Similarly, the viscous anergy increases to very low levels before the inter-blade channel, which highlights that the viscous dissipation is mainly situated inside and downstream of it. $C_{\dot{\mathcal{A}}'_\phi}$ then increases significantly inside the inter-blade channel up to 5.58 pc for $x_{TP} = 0.05m$ and keeps increasing

with a less steep slope due to viscous dissipation inside boundary layers (in the blade wake and the tip leakage vortex region). The thermal anergy evolves with a similar trend as the viscous anergy, with significantly lower values. Overall, thermal effects linked to $C_{\dot{\mathcal{X}}'_{th}}$ and $C_{\dot{\mathcal{A}}'_{\nabla T}}$ are of second order compared to mechanical effects in the flow.

High-flow condition ($\dot{m} \approx 0.98\dot{m}_{choke}$) with an isothermal casing

The exergy balance component evolution for different x_{TP} values is presented in Fig. 5, considering an isothermal casing at a temperature $T_{casing} = 288.15$K. (Bruna and Turner, 2013)

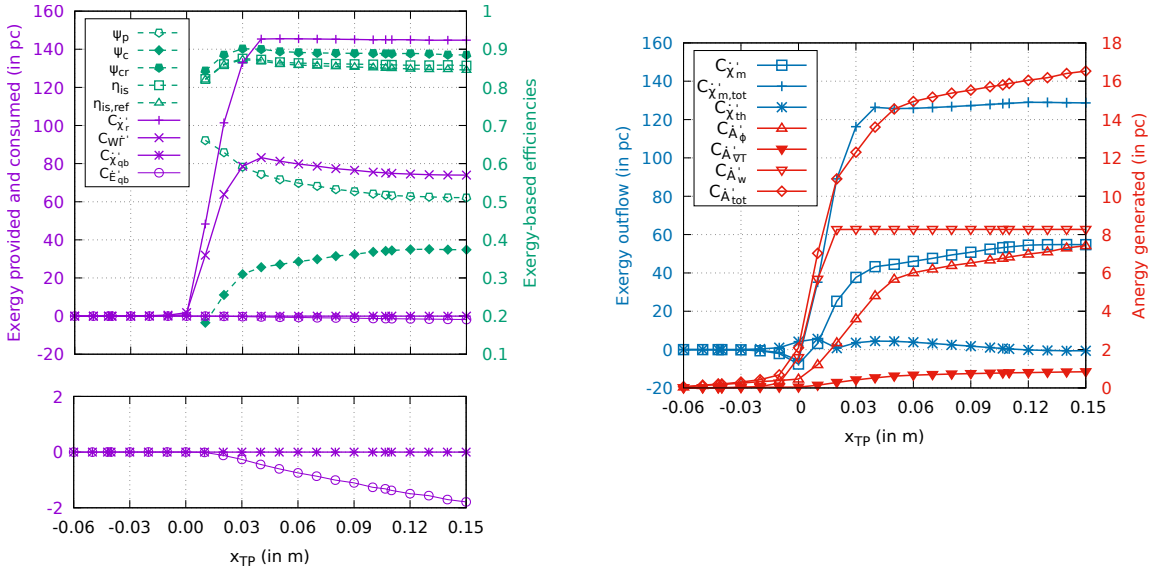

Figure 5: Exergy balance evolution at $\dot{m} \approx 0.98\dot{m}_{choke}$ for an isothermal casing.

showed that this boundary condition modification leads to a non-negligible increase of η_{is}. Thus, the isentropic efficiency corresponding to the adiabatic case (noted $\eta_{is,ref}$) is also plotted to ensure that the expected gain is obtained. The thermal exergy transferred by conduction through walls and the thermal energy associated (with $\dot{\mathcal{X}}'_{qb} = \dot{E}'_{qb} - \dot{\mathcal{A}}'_{qb}$) are represented as well.

The exergy balance components are not impacted significantly by the boundary condition modification at the casing. In particular, Fig. 5 shows that the thermal exergy exchanged by conduction through the casing stays null for every x_{TP} value. The gain of isentropic efficiency compared to the adiabatic case is yet clearly visible when the transverse plane position is moved downstream. More specifically, for $x_{TP} = 0.1067m$, the isentropic efficiency gain is equal to 0.86%, in the same order of magnitude than what is obtained by (Bruna and Turner, 2013). There is however no significant variation of ψ_{cr}, which varies by only 0.1% at the same station due to the effect of the thermal conduction on the exergy outflow. The difference of variations between ψ_{cr} and η_{is} is in fact directly linked to the difference between thermal energy and thermal exergy themselves. The additional heat transfer by conduction leads to no exchange of thermal exergy, thus leading to a limited impact on the reversible compression efficiency (which is itself due to the effects observed on other terms of the balance). Nevertheless, Fig. 5 shows that while $\dot{\mathcal{X}}'_{qb} = 0$, the associated thermal energy $\dot{E}'_{qb}$ evolves from zero to negative values when x_{TP} increases (cf. the bottom left zoom in Fig. 5). This highlights that, as the flow goes through various thermodynamic processes across the channel, its temperature increases and heat is evacuated from the control volume through the isothermal casing. The energy gain in the compressor then decreases whereas the exergy gain stays almost constant (compared to

the adiabatic case), as the process of heat evacuation through the casing holds no potential for mechanical work recovery. On the other hand, when defining η_{is}, the energy gain in the compressor is assumed to be a cost (thus the total enthalpy gain is placed at the denominator), while the numerator can be attributed to an exergy gain under specific conditions (Kotas, 1985). Thus, the increase of η_{is} is not due to a higher potential of mechanical work recovery downstream of the compressor, but rather to a lower apparent cost associated to the increase of the exergy of the flow to the same level as in the case of an adiabatic casing. The augmentation of η_{is} is then due to a heat removal process which does not hold a potential for mechanical work recovery. It does not truly correspond to a lower cost as the energy expended in the experiment that is transmitted to the flow is only of a mechanical origin (and corresponds to $\dot{\mathcal{X}}'_r$) which is not significantly impacted by these thermal transfers.

Comparison of the exergy-based characteristic for the reference and optimized geometries

In this section, the downstream plane limiting the control volume is fixed at $x_{TP} = 0.1067$m and the casing is adiabatic. $\dot{m}$ is then modified to analyze the performance of the NASA Rotor 37 under different operating conditions. The components of the exergy balance are plotted in Fig. 6 as functions of $\dot{m}$ for the reference (dotted lines) and the optimized (solid lines) geometries. The thermocompressible exergy outflow and the thermal anergy generated are not plotted (of second order compared to coefficients linked to mechanical effects).

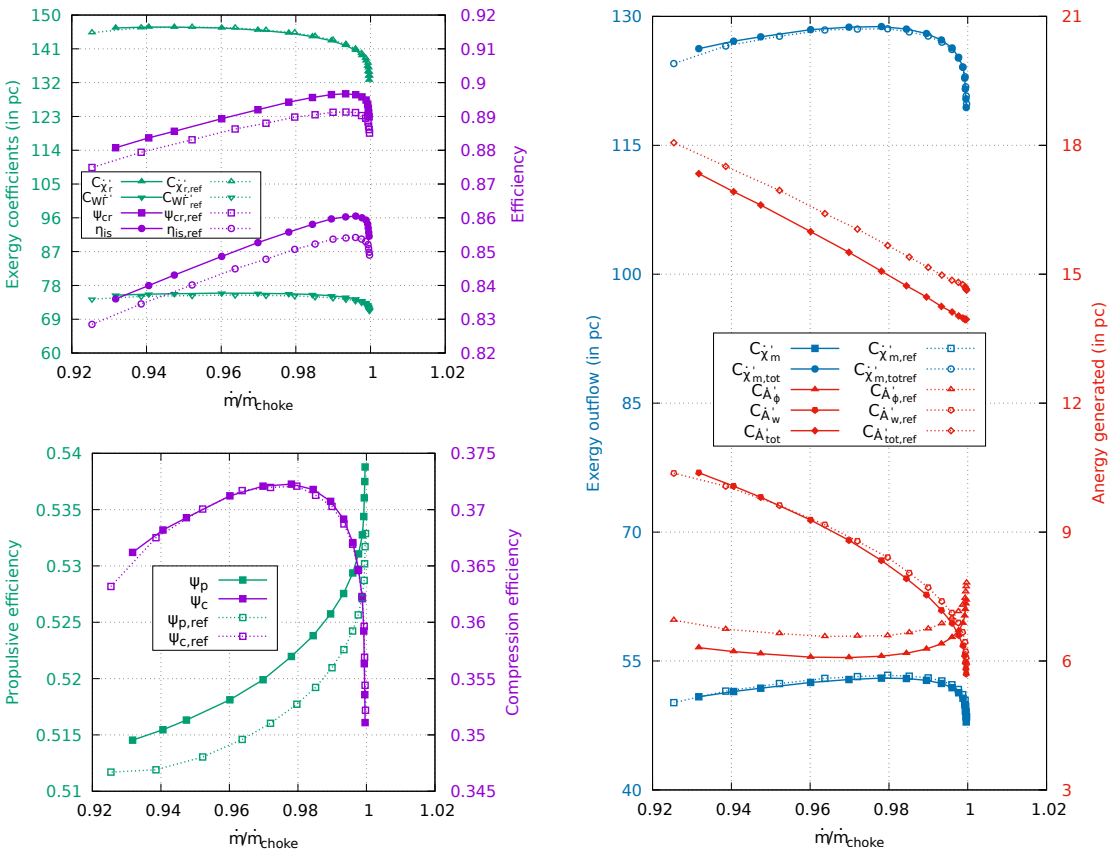

Figure 6: Comparison of the exergy balance components for several operating regimes between an optimized and the reference Rotor 37 geometries.

Let us first focus on the reference geometry coefficients. The top left graph of Fig. 6 shows that $C_{\dot{\mathcal{X}}'_{r,ref}}$ and $C_{W\dot{\Gamma}'_{ref}}$ increase slightly until $\dot{m} \approx 0.95\dot{m}_{choke}$ and $\dot{m} \approx 0.965\dot{m}_{choke}$ respec-

tively. They then decrease rapidly as the choke flow regime is approached, with the decrease being more significant for $C_{\dot{\mathcal{X}}'_{r,ref}}$ than for $C_{W\dot{\Gamma}'_{ref}}$. The latter corresponds to an increase of $\psi_{p,ref}$ which is more notable near the choke flow regime. The compression efficiency $\psi_{c,ref}$ on the other hand increases until the high-flow condition is reached, before decreasing rapidly near the blockage. The top left graph in Fig. 6 also shows that $\psi_{cr,ref}$ and $\eta_{is,ref}$ have a similar evolution, with $\psi_{cr,ref}$ values being consistently higher by 3-4%. Both figures of merit predict an optimal operating regime near choke ($\dot{m}_{opt} \approx 0.996\dot{m}_{choke}$). As discussed in previous sections, the differences observed are linked to the friction reheat effect and different sources of numerical errors.

The right graph in Fig. 6 shows the evolution of the exergy outflow components and the anergy generated inside the control volume. As $\dot{m}$ increases, both $C_{\dot{\mathcal{X}}'_{m,ref}}$ and $C_{\dot{\mathcal{X}}'_{m,totref}}$ increase until the high-flow condition is reached. They then decrease rapidly as $\dot{m}$ approaches the choke flow regime, similarly to what is observed for $C_{\dot{\mathcal{X}}'_{r,ref}}$. As for the anergy contributions, different trends are observed as $\dot{m}$ increases. First, the wave anergy decreases with a most significant reduction being obtained near choke flow conditions. This behavior is consistent with observations of (Denton, 1997), in particular due to the shock structure in the inner half of the Rotor 37 switching from a single strong bow shock at low mass flow rates to a system of two distinct shocks near choke (a bow shock and a passage shock, thus reducing the shock losses (Denton, 1993)). Second, as $\dot{m}$ increases from near-stall values, the viscous anergy decreases and stays close to its minimum level until the high-flow condition is reached. The higher values observed near stall are due to the strengthening of the blockage associated to the tip leakage vortex (Ameri, 2009) at low mass flow rates. The viscous anergy level then increases very rapidly as the compressor blockage is approached, in which case this term becomes the main source of irreversible dissipation. This increase was found to be mainly due to a higher dissipation in the inter-blade channel. These observations are confirmed by iso-surfaces of viscous anergy generation (see Fig. 7), which show that higher levels of viscous anergy generation due to the tip leakage flow are observed near stall compared to the other operating regimes. Overall, Fig. 6

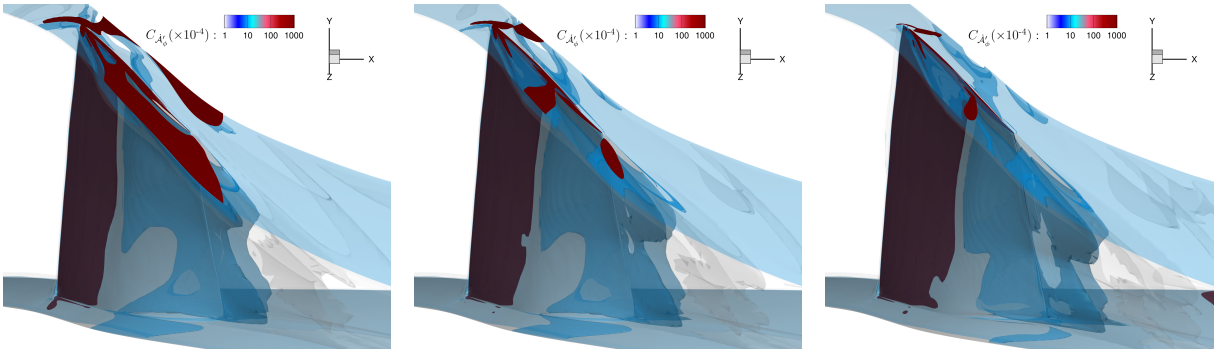

Figure 7: Iso-surfaces of $C_{\dot{\mathcal{A}}'_{\phi}}$ at $\dot{m} \approx 0.925\dot{m}_{choke}$ (left), $\dot{m} \approx 0.98\dot{m}_{choke}$ (middle) and $\dot{m} \approx \dot{m}_{choke}$ (right) for the reference geometry. The casing wall is not shown.

shows that $C_{\dot{\mathcal{A}}'_{tot,ref}}$ decreases when $\dot{m}$ increases for all the operating regimes investigated. This highlights that the optimal operating regime in terms of efficiency does not necessarily correspond to the one with minimum irreversible loss. Hence, the complete exergy balance must be considered to correctly investigate the performance of the system. Additionally, it is important to note that standard analyses focusing only on total losses would usually only identify an overall reduction as $\dot{m}$ increases. The exergy balance provides a decomposition allowing to identify the trend difference between $\dot{\mathcal{A}}'_{\phi}$ and $\dot{\mathcal{A}}'_{w}$, an effect which is masked in overall losses (e.g. $\dot{\mathcal{A}}'_{tot}$

or entropy flux).

At a second step, an investigation of the impact of the optimization on the exergy balance components is presented in Fig. 6. The main goal of the optimization is successfully achieved as an overall gain is obtained for ψ_{cr} and η_{is} over the whole characteristic. The gain is maximal near the peak efficiency, which is consistent with the optimization strategy, and lower near stall and choke flow conditions. Higher $C_{W\dot{\Gamma}'}$ values are obtained until choke flow is reached compared to the reference case, meaning that a higher forward streamwise force is obtained and more exergy has to be consumed to maintain the axial mechanical equilibrium. Close to stall, $C_{\dot{\mathcal{X}}'_r}$ is also slightly higher with the optimized geometry. For the rest of the characteristic, it is however lower than for the reference geometry, meaning that less exergy is transferred from the compressor to the fluid (which can be linked to both less exergy outflow and anergy generated). It should be noted that differences between the two geometries in terms of $C_{\dot{\mathcal{X}}'_r}$ and $C_{W\dot{\Gamma}'}$ are small but quantifiable, which is portrayed in the evolutions of ψ_p and ψ_c. The right graph in Fig. 6 shows that, at similar mass flow rates, the total mechanical exergy outflow $C_{\dot{\mathcal{X}}'_{m,tot}}$ is higher in the optimized case for most operating regimes. Near choke, it however decreases to end up at slightly lower levels compared to the reference geometry. As for the mechanical exergy outflow $C_{\dot{\mathcal{X}}'_m}$, it is lower in the optimized case for all the operating regime studied. Thus, the points where the total mechanical exergy is higher in the optimized case correspond to higher levels of $W\dot{\Gamma}'$ compared to the reference case. These observations are then complemented by the evolution of anergy generation between the two geometries. The total anergy evolution shows that less irreversible losses are obtained with the optimized geometry across the complete characteristic. The gain seems to be maximum near the peak efficiency, which is again consistent with the optimization strategy. The main benefit comes from the reduction of viscous anergy over the complete characteristic, with a decrease of this gain observed near choke. The lower reduction of total anergy near stall is then explained by the wave anergy evolution. While $C_{\dot{\mathcal{A}}'_w} < C_{\dot{\mathcal{A}}'_{w,ref}}$ for $\dot{m} > 0.95\dot{m}_{choke}$, $C_{\dot{\mathcal{A}}'_w} > C_{\dot{\mathcal{A}}'_{w,ref}}$ for $\dot{m} < 0.95\dot{m}_{choke}$. Thus, the benefits obtained on the viscous anergy near stall are partially balanced by an augmentation of losses due to the shockwave. Finally, the compression and propulsive efficiency are plotted on the bottom left graph in Fig. 6. The main improvement is observed for the propulsive efficiency over the complete characterisic, with a much lower gain on the compression efficiency. This is in line with the evolutions observed for $C_{\dot{\mathcal{X}}'_r}$, $C_{W\dot{\Gamma}'}$ and the exergy outflow.

Overall, the above discussion highlights that the effect of an optimisation performed to maximize the isentropic efficiency under several constraints is clearly depicted in the exergy balance coefficient evolution. Another optimization strategy could consist in defining the objective function and the constraints directly with the exergy balance components. A first level of complexity could consist in separating the exergy balance contributions in the definition of the optimization problem, for example by minimizing $\dot{\mathcal{X}}'_r$ while constraining the overall exergy outflow to remain at a similar level. This would in fact lead to a reduction in anergy generation in the control volume, thus improving the overall performance. Note that depending on the designer's objective, a specific anergy component can also be selected as the objective function (for example $\dot{\mathcal{A}}'_w$ could be selected if reducing the shockwave losses is the main objective). Another approach could consist in basing the objective function on the exergy-based figures of merit defined in this paper. For example, ψ_{cr} could be maximized during the optimization process, with constraints applied to individual components of the exergy balance. The friction reheat effect would then be included in the efficiency on which the optimisation is based, which should lead to a more physically-complete estimation of the compressor performance improvement.

Conclusion and perspectives

This paper presents an exergy-based performance analysis of the NASA rotor 37 test case. The behavior of the exergy balance components and of the associated figures of merit are investigated for several operating regimes in order to characterize the system's performance. The link between exergy-based efficiencies and classical figures of merit used in the turbomachinery field is investigated, and interpretations of the differences observed are provided. The case of an isothermal casing is investigated from an exergetic point of view, which allows to refine the interpretation of the gain in isentropic efficiency observed in the literature. A comparison is finally performed between the reference geometry and an in-house optimized version, by using the exergy balance to analyse sources of improvement. In terms of perspectives, as the thermal effects are accounted for in the exergy balance, the study of a turbine case would be of particular interest in the future. The exergy balance is expected to provide more detailed information on turbine performance than classical analyses, as mechanical and thermal effects can be decomposed but are contained within a single balance.

ACKNOWLEDGEMENTS

This work was funded by the French Directorate General for Civil Aviation (DGAC) through the SUBLIME and IDEFFIX conventions. The studies presented have used the elsA software, whose development is partially funded by its two co-owners ONERA and SAFRAN. The authors would like to thank Antoine Dumont and Raphaël Barrier for sharing their valuable knowledge, as well as for providing the reference/optimized geometries and computational grids analysed in this paper.

REFERENCES

Ali Ameri. NASA ROTOR 37 CFD CODE Validation Glenn-HT Code. In *47th AIAA Aerospace Sciences Meeting including The New Horizons Forum and Aerospace Exposition*, 2009. DOI: 10.2514/6.2009-1060. AIAA Paper 2009-1060.

Aurélien Arntz. *Civil aircraft aero-thermo-propulsive performance assessment by an exergy analysis of high-fidelity CFD-RANS Flow Solutions*. PhD thesis, Lille 1 University - Sciences and Technologies, 2014. URL https://hal.archives-ouvertes.fr/tel-01113135.

Christophe Benoit, Stéphanie Péron, and Sâm Landier. Cassiopee: A CFD pre- and post-processing tool. *Aerospace Science and Technology*, 45:272–283, 2015. DOI:10.1016/j.ast.2015.05.023.

Ilyès Berhouni, Didier Bailly, and Ilias Petropoulos. On the adaptation of the exergy definition in the field of aerodynamics. In *57th 3AF International Conference on Applied Aerodynamics*, 2023a. Paper AERO2023-18.

Ilyès Berhouni, Didier Bailly, and Ilias Petropoulos. Extension of the exergy balance to rotating reference frames: Application to a propeller configuration. *AIAA Journal*, 2023b. DOI: 10.2514/1.J062216. Article in advance.

Dario Bruna and Mark G. Turner. Isothermal boundary condition at casing applied to the rotor 37 transonic axial flow compressor. *Journal of Turbomachinery*, 135(3), 2013. DOI:10.1115/1.4007569.

Daniel Burdett and Thomas Povey. Analysis of averaging methods for nonuniform total pressure fields. *Journal of Turbomachinery*, 144(5), 2022. DOI:10.1115/1.4053020.

Laurent Cambier, Sébastien Heib, and Sylvie Plot. The Onera elsA CFD software: input from research and feedback from industry. *Mechanics & Industry*, 14(3):159–174, 2013. DOI: 10.1051/meca/2013056.

Yunus A. Çengel and Michael A. Boles. *Thermodynamics: An Engineering Approach.* 2015. 8th edition, New York: McGraw-Hill.

John D. Denton. Loss Mechanisms in Turbomachines. In *Volume 2: Combustion and Fuels; Oil and Gas Applications; Cycle Innovations; Heat Transfer; Electric Power; Industrial and Cogeneration; Ceramics; Structures and Dynamics; Controls, Diagnostics and Instrumentation; IGTI Scholar Award*. American Society of Mechanical Engineers, 1993. DOI:10.1115/93-gt-435.

John D. Denton. Lessons from rotor 37. *Journal of Thermal Science*, 6(1):1–13, 1997. DOI:10.1007/s11630-997-0010-9.

Maxime Fiore. *Influence of cavity flow on turbine aerodynamics*. PhD thesis, ISAE-Institut Supérieur de l'Aéronautique et de l'Espace, 2019. URL http://www.theses.fr/2019ESAE0013.

Chunill Hah. Large eddy simulation of transonic flow field in NASA rotor 37. In *47th AIAA Aerospace Sciences Meeting including The New Horizons Forum and Aerospace Exposition*, 2009. DOI:10.2514/6.2009-1061. AIAA Paper 2009-1061.

Tadeusz J. Kotas. Chapter 4 - Exergy analysis of simple processes. In *The Exergy Method of Thermal Plant Analysis*. Elsevier, 1985. DOI:10.1016/b978-0-408-01350-5.50011-8.

Robert J. Miller. Mechanical work potential. In *Volume 6A: Turbomachinery*, Turbo Expo: Power for Land, Sea, and Air. American Society of Mechanical Engineers, 2013. DOI:10.1115/gt2013-95488.

Royce D. Moore and Lonnie Reid. *Performance of single-stage axial-flow transonic compressor with rotor and stator aspect ratios of 1.19 and 1.26 respectively, and with design pressure ratio of 2.05*. National Aeronautics and Space Administration, 1980. URL https://ntrs.nasa.gov/citations/19800012840. NASA Technical Paper 1659.

Jacques Peter, Florent Renac, Antoine Dumont, and Michaël Méheut. Discrete adjoint method for shape optimization and mesh adaptation in the elsA code. status and challenges. In *50th 3AF International Conference on Applied Aerodynamics*, 2015.

Lonnie Reid and Royce D. Moore. Design and overall performance of four highly loaded, high speed inlet stages for an advanced high-pressure-ratio core compressor. Technical report, 1978. URL https://ntrs.nasa.gov/citations/19780025165. NASA Technical Paper 1337.

Kenneth Lee Suder. *Experimental investigation of the flow field in a transonic, axial flow compressor with respect to the development of blockage and loss*. PhD thesis, Case Western Reserve University, 1996. URL https://ntrs.nasa.gov/api/citations/19970001675/downloads/19970001675.pdf.

Garret N. Vanderplaats. Dot optimization. http://www.vrand.com/products/dot-optimization/, . Accessed: 2022-11-24.